

Cosmological Constraints from Combining Galaxy Surveys and Gravitational Wave Observatories

E. L. Gagnon^{*, 1, 2}, D. Anbajagane^{1, 2}, J. Prat^{1, 2}, C. Chang^{1, 2}, J. Frieman^{1, 2, 3}

¹ *Department of Astronomy and Astrophysics, University of Chicago, Chicago, IL 60637, USA*

² *Kavli Institute for Cosmological Physics, University of Chicago, Chicago, IL 60637, USA and*

³ *Fermi National Accelerator Laboratory, Batavia, IL 60510, USA*

Version December 29, 2023

ABSTRACT

Spatial variations in survey properties due to both observational and astrophysical selection effects generate substantial systematic errors in large-scale structure measurements in optical galaxy surveys on very large scales. On such scales, the statistical sensitivity of optical surveys is also limited by their finite sky coverage. By contrast, gravitational wave (GW) sources appear to be relatively free of these issues, provided the angular sensitivity of GW experiments can be accurately characterized. We quantify the expected cosmological information gain from combining the forecast LSST 3×2pt analysis (the combination of three two-point correlations of galaxy density and weak lensing shear fields) with the large-scale auto-correlation of GW sources from proposed next-generation GW experiments. We find that in Λ CDM and w CDM models, there is no significant improvement in cosmological constraints from combining GW with LSST 3×2pt over LSST alone, due to the large shot noise for the former; however, this combination does enable an estimated $\sim 6\%$ constraint on the linear galaxy bias of GW sources. More interestingly, the optical-GW data combination provides tight constraints on models with primordial non-Gaussianity (PNG), due to the predicted scale-dependent bias in PNG models on large scales. Assuming that the largest angular scales that LSST will probe are comparable to those in Stage III surveys ($\ell_{\min} \sim 50$), the inclusion of next-generation GW measurements could improve constraints on the PNG parameter f_{NL} by up to a factor of $\simeq 6.6$ compared to LSST alone, yielding $\sigma(f_{\text{NL}}) = 8.5$. These results assume the expected capability of a network of Einstein Telescope-like GW observatories, with a GW detection rate of 10^6 events/year. We investigate the sensitivity of our results to different assumptions about future GW detectors as well as different LSST analysis choices.

1 INTRODUCTION

As cosmic surveys continue to grow in scale, they enable measurements of large-scale structure (LSS) with ever-greater precision that in principle translate into ever-tighter cosmological constraints. The current state of the art in extracting cosmological information from large photometric surveys is the so-called “3×2pt” analysis, which combines the information from three two-point correlation functions: the galaxy auto-correlation function, the weak lensing (cosmic shear, or shear-shear) correlation function, and the galaxy-shear correlation function. All three major Stage III photometric survey

collaborations¹ have carried out such analyses: the Dark Energy Survey (DES, [Abbott et al. 2018, 2022](#)), the Kilo-Degree Survey (KiDS, [Heymans et al. 2021](#)) and the Hyper Suprime-Cam Subaru Strategic Program (HSC-SPP, [Sugiyama et al. 2023](#)).

While these correlations can be measured over a very wide range of length scales, so far cosmological inference from them has focused on intermediate spatial scales only – typically between $\sim 8h^{-1}$ Mpc and $\sim 100h^{-1}$ Mpc – due to limitations at both larger and smaller scales. Smaller scale measure-

¹ The Stage-III and Stage-IV classification was introduced in the Dark Energy Task Force report ([Albrecht et al. 2006](#)), where Stage-III refers to the dark energy experiments that started data taking in the 2010s and Stage-IV to those that started or will start in the 2020s.

*: Corresponding author: elgagnon@uchicago.edu

ments, although having higher signal-to-noise, are challenging to model due to nonlinearities in the density field, uncertainties in the galaxy-dark matter connection, and complex baryon physics (Wechsler & Tinker 2018; Martinelli et al. 2021; Chen et al. 2023). Structure on very large scales is easier to model, but the measurements suffer from observational and astrophysical systematic effects. For example, in the Year 3 (Y3) DES galaxy clustering measurements, it was shown that significant corrections (larger than 5σ , where σ is the measurement uncertainty) had to be made to the measurements due to observational systematic effects on angular scales larger than 250 arcmin ($\ell \lesssim 45$), as shown in Fig. 2 of Rodríguez-Monroy et al. (2022). To fully exploit the cosmological information coming from galaxy surveys, it is imperative to re-examine some of these scale limitations with new tools and data that become available over time.

While there has been substantial recent work employing emerging techniques and simulations to harness information from small scales, e.g., Miyatake et al. (2022); Kobayashi et al. (2022); Yuan et al. (2022); Miyatake et al. (2023); Aricò et al. (2023); Dvornik et al. (2023); Lange et al. (2023), this paper focuses on extracting information from the largest scales. The Vera C. Rubin Observatory’s Legacy Survey of Space and Time (LSST, Ivezić et al. 2019) will enable a 3×2 pt analysis on large scales of unprecedented statistical power. But as an optical photometric survey, it will be subject to the same sources of astrophysical and observational systematics as Stage III surveys. Therefore, we consider using gravitational wave (GW) sources as a complementary probe of very large-scale structure and combining GW and LSST measurements.

The rationale of this approach is that on very large scales, GW observations suffer significantly less from observational and astrophysical systematic effects compared to optically selected galaxies, and their selection function can be known extremely well (Schutz 2011; Chen et al. 2017) – unlike electromagnetic signals, GWs are not affected by issues such as spatially varying Galactic dust extinction, variations in survey depth due to time-varying observing conditions and spatially varying star density, and other similar phenomena. In addition, gravitational waveforms are a direct prediction of general relativity (eg. Finn & Chernoff 1993). Moreover, a distinctive feature of GW observations is their full sky coverage, a significant advantage over ground-based electromagnetic observations, which typically have limited sky coverage due to their geographic location and the need to discard a substantial portion of the sky (25 – 40%) to obtain cosmological information, due to Galactic foregrounds. GW sources can thus be used to robustly measure clustering on very large angular scales.

With a limited number of terrestrial GW detectors simultaneously operating, most GW sources cannot be localized on

the sky with an angular precision better than a few square degrees. As a result, the angular clustering of GW sources cannot be measured on small scales. This is not a limitation for our analysis, however, as LSST will provide high signal-to-noise measurements on such scales.

As we will see, combining LSST 3×2 pt with GW clustering also allows us to break the degeneracy between the bias of GW host-galaxy sources, b_{GW} , and the amplitude of mass clustering in the universe, σ_8 , yielding interesting constraints on b_{GW} . This is of interest in its own right, since the bias of GW host-galaxies is not currently well determined (e.g. Adhikari et al. 2020; Zheng et al. 2023), and constraining it will have implications for understanding the formation channel of GW sources (Scelfo et al. 2018).

Previous works have studied the clustering of GW sources and its cross-correlation with galaxy positions. Bosi et al. (2023) and Scelfo et al. (2023) considered GW \times LSS cross-correlations to constrain cosmological models, particularly modified gravity theories. Bera et al. (2020) used cross-correlations to infer H_0 , and Mukherjee et al. (2021) constrained cosmological parameters including the GW bias. Scelfo et al. (2020) and Calore et al. (2020) studied such correlations to gain an astrophysical understanding of GW sources. Shao et al. (2022) and Yang & Hu (2023) studied the impact of more realistic observational effects on measuring and modeling GW clustering. Balaudo et al. (2023), and Mpetha et al. (2023) considered the weak lensing of GW events to constrain extended cosmological models. Some studies have also cross-correlated GW sources with other large-scale structure tracers such as supernovae (Libanore et al. 2022) and HI intensity mapping (Scelfo et al. 2022).

Our paper takes a different direction from previous work in two ways: 1) we study the complementary combination of GW clustering and LSST 3×2 pt, and 2) we explore constraints on both the standard Λ CDM and w CDM cosmological models as well as primordial non-Gaussianity (PNG), specifically, the local PNG model parametrized by f_{NL} . To date, the *Planck* cosmic microwave background (CMB) measurements have provided the most stringent constraints on PNG (Planck Collaboration 2020), but these measurements are already near the cosmic variance limit of precision, so future CMB experiments are unlikely to significantly improve upon these results. Thus, the new frontier for constraining PNG lies in large-scale surveys of the galaxy and matter distributions. We note that Namikawa et al. (2016) also considered GW clustering for constraining f_{NL} , but they did not combine GW with galaxy 3×2 pt analyses, which offers some major advantages that we explore in this work, such as the self-calibration of the GW host-galaxy bias.

This paper is structured as follows. In Sec. 2, we present

the theoretical framework, in Sec. 3, we describe the analysis setups for galaxy surveys and GWs, and in Sec. 4 we present the results of our analysis. We conclude in Sec. 5.

2 MODELING

2.1 Large-Scale Structure in Λ CDM and w CDM

Given the limited photometric redshift precision achieved by imaging surveys that employ a handful of optical passbands, the lowest order LSS clustering statistic commonly measured is the 2D angular correlation function or equivalently the 2D angular power spectrum, $C^{ij}(\ell)$, within and between photometric-redshift bins i, j . Here, ℓ is the 2D multipole moment, which is roughly related to angular separation on the sky, θ , by $\ell \sim \pi/\theta$. In the 3×2 pt analysis, we focus on three angular power spectra: the auto-correlation of a foreground (or lens) galaxy population, C_{gg} , the cross-correlation between lens-galaxy position and source-galaxy shear, C_{gy} , also known as galaxy-galaxy lensing, and the auto-correlation of source-galaxy shear, C_{yy} , also known as cosmic shear.

We follow common practice in using the first-order Limber approximation (LoVerde & Afshordi 2008) to relate the angular galaxy-galaxy, galaxy-shear, and shear-shear power spectra to the corresponding 3D power spectra,

$$C_{\text{gg}}^{ij}(\ell) = \int d\chi \frac{N_l^i(\chi) N_l^j(\chi)}{\chi^2} P_{\text{gg}}\left(k = \frac{\ell + 1/2}{\chi}, z(\chi)\right), \quad (1a)$$

$$C_{\text{gy}}^{ij}(\ell) = \int d\chi \frac{N_l^i(\chi) q_s^j(\chi)}{\chi^2} P_{\text{gm}}\left(k = \frac{\ell + 1/2}{\chi}, z(\chi)\right), \quad (1b)$$

and

$$C_{\text{yy}}^{ij}(\ell) = \int d\chi \frac{q_s^i(\chi) q_s^j(\chi)}{\chi^2} P_{\text{mm}}\left(k = \frac{\ell + 1/2}{\chi}, z(\chi)\right). \quad (1c)$$

Here, $P_{\text{mm}}(k, z)$ is the 3D matter power spectrum, $P_{\text{gm}}(k, z)$ is the 3D (lens) galaxy-matter power spectrum, and $P_{\text{gg}}(k, z)$ is the 3D lens-galaxy power spectrum, χ is the comoving distance, z is redshift, and N_l^i describes the true redshift distribution of the lens-galaxy population in the i th photometric-redshift bin:

$$N_l^i(\chi) = \frac{n_l^i(z)}{\bar{n}_l^i} \frac{dz}{d\chi}, \quad (2)$$

where n_l^i is the lens-galaxy redshift distribution, and \bar{n}_l^i is the mean number density of lens galaxies. In addition, q_s^i is the lensing kernel of the source-galaxy population:

$$q_s^i(\chi) = \frac{3H_0^2 \Omega_m}{2c^2} p(\ell) \frac{\chi}{a(\chi)} g(\chi), \quad (3)$$

where a is the scale factor, $p(\ell)$ is the ℓ -dependent prefactor in the lensing observables due to the spin-2 nature² of the shear, and $g(\chi)$ is the lensing efficiency kernel:

$$g(\chi) = \int_{\chi}^{\chi_h} d\chi' \frac{n_s^i(z)}{\bar{n}_s^i} \frac{dz}{d\chi'} \frac{\chi' - \chi}{\chi'}, \quad (4)$$

where $n_s^i(z)$ is the redshift distribution of the source galaxies in the i th photometric redshift bin, \bar{n}_s^i is the mean number density of the source galaxies, and χ_h is the comoving distance to the horizon.

The Limber approximation assumed in Eqn.(1) is known to break down at large angular scales, that is, for small ℓ . This is particularly the case if the kernel functions $N_l^i(\chi)$ and $q_s^i(\chi)$ are narrowly peaked functions of χ . Given the relatively broad redshift bins we adopt in this analysis (see Fig. 2) and scaling from the results in LoVerde & Afshordi (2008), we expect this to lead to a relatively small error in our analysis for angular multipoles $\ell \gtrsim 3$, one outweighed by the significant savings in computation time. As an additional complication, the mean of any estimator of C_ℓ in a survey of finite angular extent Θ will differ appreciably from the theoretical values in Eqn. (1) for multipoles $\ell < \pi/\Theta$. In practice, for the analysis set-up we consider, this is a very small correction, since GW surveys are effectively all-sky, and π/Θ_{LSST} is comfortably below the minimum angular multipole that we consider in the analysis of LSST data.

Throughout the paper, if not otherwise specified, we take the matter power spectrum P_{mm} to be that given by the spatially flat 5-parameter Λ CDM model with fiducial parameters $\Omega_c = 0.22$, $\sigma_8 = 0.8$, $\Omega_b = 0.0448$, $h = 0.71$, and $n_s = 0.963$. We also consider the w CDM model, with an additional free parameter given by the (constant) equation of state parameter of dark energy, w_0 , with fiducial value $w_0 = -1$. The non-linear regime of the matter power spectrum is modeled using the HALOFIT prescription (Takahashi et al. 2012). Since we are working on large length scales, we assume a linear, scale-independent galaxy bias model for the lens galaxies, in which

$$P_{\text{gg}}(k, z) = b_g(z) P_{\text{gm}}(k, z) = b_g^2(z) P_{\text{mm}}(k, z). \quad (5)$$

For GW sources, the populations of lens galaxies in Eqns. (1a) and (2) are replaced by those of GW sources, and we assume that the host galaxies of GW sources are also linearly biased with respect to the matter distribution but with a different bias parameter, $b_{\text{GW}}(z)$. Assuming that GW sources can be typically localized to within an area of size Θ_{GW}^2 , we only consider clustering of GW sources on angular scales $\ell < \pi/\Theta_{\text{GW}}$, so that localization corrections to the estimator for Eqn. (1a) should be very small.

² Here we use $p(\ell) = (\ell + 1/2)^{-2}$, which corresponds to the 1st order extended Limber flat projection (ExtL1F1), as defined in table 1 from Kilbinger et al. (2017)

To calculate angular power spectra and their covariances (see §3), we use the new differentiable cosmology library `jax_cosmo` (Campagne et al. 2023) to perform our analysis. Testing a variety of setups (see Sec. 3.1, 3.2) is core to our investigation, and `jax_cosmo`'s differentiable functions provide the crucial ability to rapidly perform Fisher forecasts in a robust and stable way.

2.2 Primordial Non-Gaussianity and f_{NL}

In addition to the canonical Λ CDM and w CDM models, we consider Λ CDM models with non-Gaussian initial conditions. Inflation is an epoch of rapid expansion in the early Universe that is thought to generate the primordial density fluctuations that subsequently evolve into the structures observed today. In the simplest inflation models involving a single, weakly coupled scalar field, the initial density perturbations are predicted to be very close to Gaussian random fields. In models with multiple scalar fields, the initial perturbations can be (potentially measurably) non-Gaussian.

We focus on models with local-type primordial non-Gaussianity (PNG) (Byrnes & Choi 2010), in which the initial conditions for the gravitational potential are given by

$$\Phi(\vec{x}) = \phi(\vec{x}) + f_{\text{NL}}(\phi(\vec{x})^2 - \langle \phi^2 \rangle), \quad (6)$$

where $\Phi(\vec{x})$ is the gravitational potential, $\phi(\vec{x})$ is a Gaussian field, and f_{NL} is a parameter that characterizes the amplitude of the PNG. In the simplest single-field inflation models, we generically expect $f_{\text{NL}} \ll 1$, so any indication of $f_{\text{NL}} > 1$ would imply that multiple fields were present during inflation (Byrnes & Choi 2010; Achúcarro et al. 2022).

PNG alters the behavior of the galaxy bias and causes galaxies to exhibit a scale-dependent bias with an amplitude that grows on large scales (Dalal et al. 2008); to lowest order, the galaxy bias in Eqn. (5) is replaced by

$$b_{\text{g}}(z) \rightarrow b_{\text{g}}(z) + b_{f_{\text{NL}}}(k, z) \quad (7)$$

where the additional scale-dependent bias term is given by

$$b_{f_{\text{NL}}}(k, z) = 3\delta_c(b_{\text{g}}(z) - 1) \frac{f_{\text{NL}}}{k^2} \left(\frac{\Omega_m H_0^2}{c^2 D(z) T(k)} \right). \quad (8)$$

Here, $\delta_c = 1.686$ is the critical threshold for halo collapse in the spherical collapse model, $D(z)$ is the linear growth factor (relative to the present), and $T(z)$ is the Λ CDM transfer function. The additional bias term grows towards large-scales, as it is proportional to $b_{f_{\text{NL}}} \propto 1/k^2$ (Dalal et al. 2008). Formally, the choice above of $(b_{\text{g}} - 1)$ can be generalized to $(b_{\text{g}} - p)$, where p is some constant. Most works employ $p = 1$, which is derived by assuming universality of the halo mass function. However, there are motivations for selecting other choices for p as well (Barreira 2020). We employ $p = 1$ to be consistent

with previous works. Alternative choices of p that are higher (lower) than this value will result in weaker (stronger) f_{NL} constraints, since lower values of p increase the scale-dependent bias, $b_{f_{\text{NL}}}$, for galaxies with $b_{\text{g}} > 1$.

To leading order, f_{NL} impacts structure formation only through the bias terms in P_{gg} and P_{gm} , and we do not include its impact on the matter power spectrum itself. This is a good approximation for linear/quasi-linear scales, as the f_{NL} -based correction goes as $\Delta P_{\text{mm}}/P_{\text{mm}} \sim f_{\text{NL}} \times 10^{-5}$. For values of $f_{\text{NL}} \sim O(10)$, as found in our constraints below, this correction is completely subdominant. However, simulations show that the impact of f_{NL} on the matter power spectrum is most prominent on non-linear scales (Coulton et al. 2023; Anbajagane et al. 2023), since the non-Gaussianity of the initial density field changes the abundance of massive halos, which impacts the matter and halo power spectrum on small scales. In principle, this means that our analysis underestimates the full impact of f_{NL} and thus overestimates the expected error on it. Anbajagane et al. (2023, see their Table 3) show that a lensing-only analysis of LSST Year 10, with realistic scale cuts, leads to constraints of $\sigma(f_{\text{NL}}) = 92$. This is broader than the constraints on f_{NL} found in our analysis below, which indicates that the inclusion of f_{NL} in the matter power spectrum would have negligible impact on our constraints compared to the signal due to scale-dependent bias.

Our analysis of PNG models uses a modified version of the `jax_cosmo` library that includes the f_{NL} signatures on the bias above³. An illustration of this effect on weak lensing and galaxy clustering observables is shown in Fig. 1, where we see that the effect is most prominent in the galaxy auto-correlation on large scales. The tightest current bounds on f_{NL} come from *Planck*, with $f_{\text{NL}} = -0.9 \pm 5.1$, and current LSS measurements provide $\sigma(f_{\text{NL}}) \sim 25-50$. Forecasts indicate that future galaxy surveys have the statistical power to decrease this by 1-2 orders of magnitude (Barreira 2022; Achúcarro et al. 2022). We extend these past efforts by including other tracer fields, namely the GW sources, and by including weak lensing to self-calibrate the galaxy bias parameters and further constrain the w CDM and Λ CDM cosmological parameters, which in turn improve the marginalized constraints on f_{NL} .

3 ANALYSIS SETUP

In this section, we specify the different sample characteristics and parameter priors that we use for the forecasts. In Sec. 3.1, we describe the samples from LSST, in Sec. 3.2 we do the same for the samples from GW observations, and in Sec. 3.3 we describe the procedure we use to compute angular correlation functions and Fisher matrices and predict the constraining power of each of the setups.

³ https://github.com/DhayaaAnbajagane/jax_cosmo.git

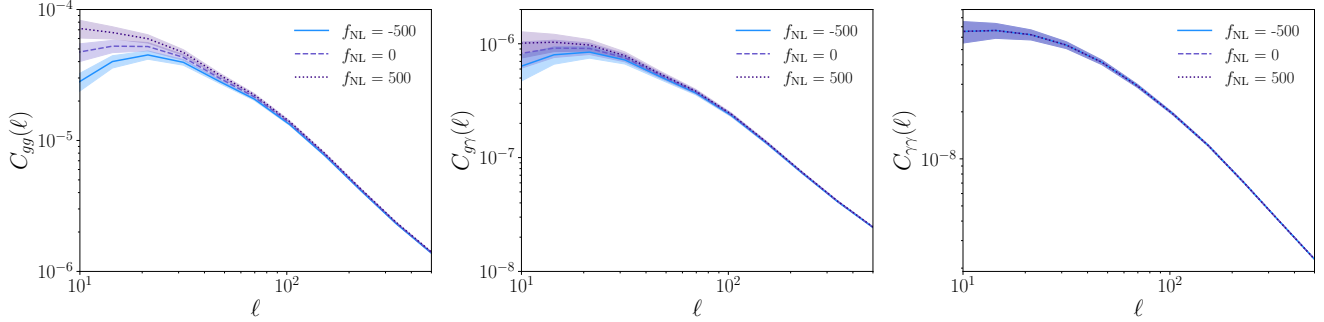


Figure 1. Lens-galaxy angular correlation function (left), galaxy-shear cross-correlation (middle), and shear-shear correlation (right), for Λ CDM models with 3 different values of f_{NL} , for galaxies in lens bin 3 and source bin 5 of the LSST Y10 3x2pt setup (see Section 3.1). Extreme values of f_{NL} are used here to illustrate the nature of the change in $C(\ell)$ shape; error bands are from Eqn. 10. We use a scale range of $10 < \ell < 500$ divided into 10 log-spaced bins.

3.1 Galaxy Surveys: The LSST Y10 setup

To generate the 3x2pt data vector we consider a survey corresponding to the LSST Year 10 setup covering 14,300 deg^2 of extragalactic (high Galactic latitude) sky, which corresponds to a fraction of the sky $f_{\text{sky}} = 0.3466$. Galaxies are divided into source and lens populations – sources are objects for which we use both position and shape information, and lenses are objects for which we use only the position information. There is overlap between the two sets of objects, as some galaxies fall into both samples. We show the true redshift distributions for each of the 10 lens and 5 source tomographic photo-z bins in the first two panels of Fig. 2. The overall $n(z)$ distribution is modeled as in Zhang et al. (2022):

$$\frac{dN}{dz} \propto z^2 \exp[-(z/z_0)^\alpha], \quad (9)$$

with $(z_0, \alpha) = (0.26, 0.90)$ for lenses and $(0.11, 0.68)$ for sources. The lens distribution is separated into 10 equipopulated bins, which are convolved with Gaussians of width corresponding to the expected photo-z precision $-0.03(1+z)$ for lenses and $0.05(1+z)$ for sources.

In Table 1, we list the peak redshift, total galaxy surface number density, and the fiducial value of the linear galaxy bias for each lens redshift bin and the assumed shape noise (intrinsic variation in the ellipticity of source galaxies) for source galaxies. The source bins have been chosen to have the same surface number density in each bin. These values are taken from the LSST DESC Science Requirement Document (DESC SRD, The LSST Dark Energy Science Collaboration (2018)). We implicitly assume uninformative priors on the cosmological parameters and on the galaxy bias parameters.

In Fig. 1 we show the forecast Λ CDM 2D angular power spectrum for LSST Year 10 lens bin 3 and source bin 5 for each of the probes we use for the 3x2pt analysis: galaxy clustering (C_{gg}), galaxy-galaxy lensing ($C_{\text{g}\gamma}$) and cosmic shear ($C_{\gamma\gamma}$).

For the uncertainties, we assume a Gaussian covariance matrix, the diagonal elements ($i = j$) of which are given by

$$\text{Cov}(C_{\text{gg}}(\ell)) = \frac{2}{(2\ell + 1)f_{\text{sky}} \Delta\ell} \left(C_{\text{gg}}(\ell) + \frac{1}{n_{\text{gal}}} \right)^2, \quad (10a)$$

$$\text{Cov}(C_{\gamma\gamma}(\ell)) = \frac{2}{(2\ell + 1)f_{\text{sky}} \Delta\ell} \left(C_{\gamma\gamma}(\ell) + \frac{\sigma_e^2}{n_{\text{gal}}} \right)^2, \quad (10b)$$

$$\text{Cov}(C_{\text{g}\gamma}(\ell)) = \frac{1}{(2\ell + 1)f_{\text{sky}} \Delta\ell} \left[C_{\text{g}\gamma}(\ell)^2 + \left(C_{\text{gg}}(\ell) + \frac{1}{n_{\text{gal}}} \right) \left(C_{\gamma\gamma}(\ell) + \frac{\sigma_e^2}{n_{\text{gal}}} \right) \right], \quad (10c)$$

where $\Delta\ell$ is the width of the chosen ℓ -binning, n_{gal} is the surface number density of lens or source galaxies in the i th redshift bin, and σ_e is the shape noise for the source galaxies. We generate angular power spectra and compute the covariance matrix using the `jax_cosmo` library.

The covariance of the angular power spectra comes from two effects: cosmic variance and shot or shape noise. The cosmic variance term is proportional to the signal, $C(\ell)$, and increases at larger scales. Shot noise in galaxy clustering and shape noise in cosmic shear are inversely proportional to galaxy number density n_{gal} – as the number density of observed objects increases, the shot/shape noise component decreases. In the left panel of Fig. 3 we show the diagonal elements of the gg covariance matrix for LSST Y10 lens bin 7, with the separate shot noise and cosmic variance terms. For LSST Y10 lenses, cosmic variance dominates by several orders of magnitude over shot noise for all scales of interest, due to the relatively high number density (large depth) of the sample.

3.1.1 Range of scales

As discussed in the Introduction, cosmological analyses of LSS cover a limited range of length or angular scales. Table 2

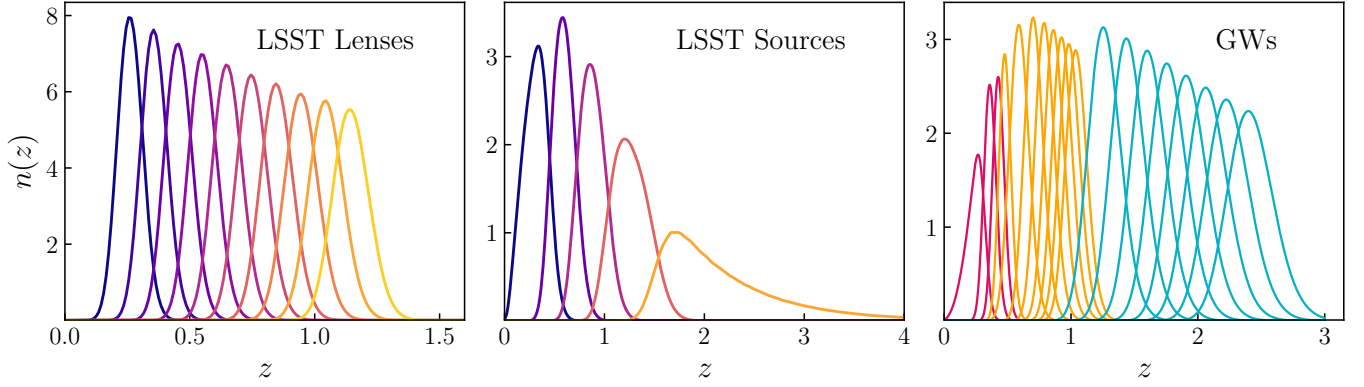


Figure 2. $n(z)$ distributions for LSST Y10 lenses, LSST Y10 sources, and the three GW detector network setups. The binning for each GW setup includes the bins of the setup before it (e.g., Setup 3 is composed of the Setup 1 bins (pink), the bins added in Setup 2 (orange), and the bins added in Setup 3 (blue)). The distributions are normalized such that they integrate to unity and therefore are not representative of the orders of magnitude difference in number density between the LSST and GW samples.

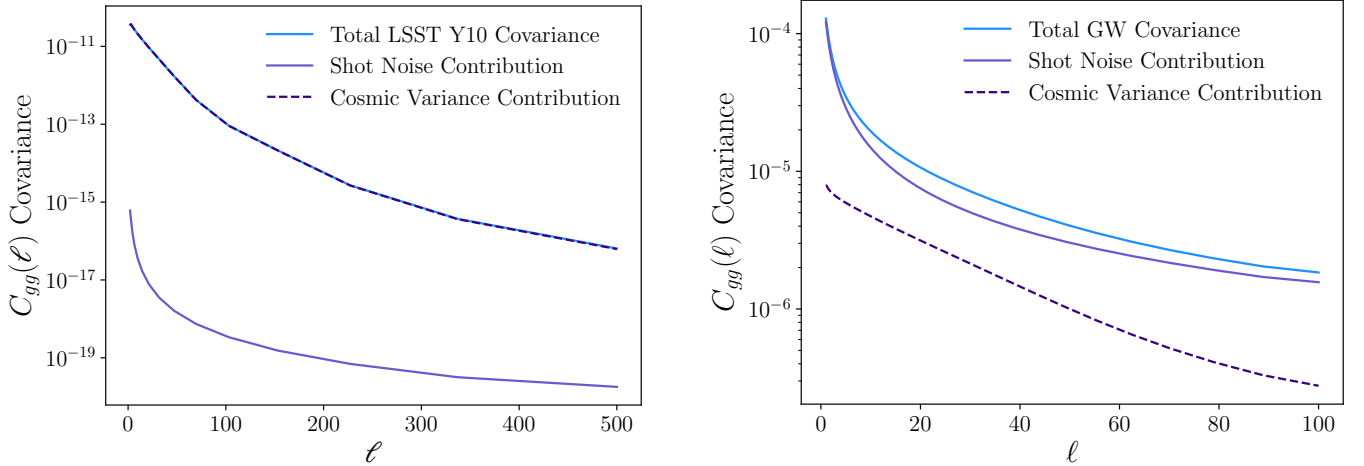


Figure 3. Galaxy clustering covariance for LSST lens bin 7 (left) and for the optimistic (Setup 3) GW bin 6 (right). Cosmic variance is the dominant source of covariance for the LSST Y10 lens bin due to the high number density in the survey. The number density of GW events is orders of magnitude lower, so that shot noise dominates and leads to an overall greater covariance.

summarizes the large-scale cuts that have been used in recent LSS analyses of Stage III surveys. These cuts are imposed for two main reasons: (i) given the limited sky coverage of these surveys, especially for HSC and KiDS, there are few to no accessible modes on very large scales, leading to very large uncertainties; (ii) observational systematics due to Galactic foregrounds and varying observing conditions have been shown to have the biggest impact on the largest scales. There is currently ongoing effort to develop methodological improvements to mitigate and control the impacts of these systematic effects on large scales. If this campaign does not succeed, then large scales will need to be discarded or downweighted in upcoming analyses.

Given the Stage III analyses, we choose $\ell_{\min} = 50$ as the fiducial value for the LSST 3 \times 2pt forecasts when we combine with GW clustering at very large scales. This cutoff corresponds approximately to the maximum of 250 arcmin that was used in the DES Y3 3 \times 2pt analysis. In the analysis below, we also explore both larger and smaller ℓ_{\min} values. Larger values could potentially be needed if the corrections for systematic effects on large scales are not found to be robust enough, particularly given the smaller statistical errors expected from LSST. We also explore the constraining power for lower ℓ_{\min} values to understand the gain that would be possible from improved control of systematic effects on large scales.

On small scales, we choose the ℓ_{\max} values (see Table 1) for

LSST Y10 Baseline Setup					
Bin	z_{peak}	Number Density (arcmin^{-2})	Galaxy Bias	ℓ_{min}	ℓ_{max}
Lens					
1	0.255	2.63	1.09	50	217
2	0.355	3.54	1.15	"	294
3	0.455	4.1	1.21	"	369
4	0.545	4.32	1.27	"	432
5	0.645	4.29	1.33	"	499
6	0.745	4.08	1.4	"	562
7	0.845	3.76	1.46	"	622
8	0.945	3.39	1.53	"	679
9	1.045	2.99	1.6	"	732
10	1.145	2.6	1.67	"	783
Source					
		Shape Noise			
1	0.335	5.4	0.26	50	500
2	0.585	"	"	"	"
3	0.855	"	"	"	"
4	1.195	"	"	"	"
5	1.675	"	"	"	"

Table 1. LSST Y10 baseline setup. ℓ_{max} values for the lenses derive from the small-scale analysis cut $k_{\text{max}} = 0.3h/\text{Mpc}$. Number density and shape noise are constant across source-galaxy bins by design.

	Large-scale cuts	Effective ℓ_{min}
DES Y3 (Abbott et al. 2022)		
$\xi_+(\theta)$	$\theta < 250'$	43
$\xi_-(\theta)$	$\theta < 250'$	43
$\gamma_t(\theta)$	$\theta < 250'$	43
$w(\theta)$	$\theta < 250'$	43
KiDS 1000 (Heymans et al. 2021)		
$C_{\gamma\gamma}(\ell)$	$\ell > 100$	100
$C_{\gamma g}(\ell)$	$\ell > 100$	100
HSC Y3 (Sugiyama et al. 2023)		
$\xi_+(\theta)$	$\theta < 50'$	216
$\xi_-(\theta)$	$\theta < 105'$	103
$\Delta\Sigma(R)$	$R < 30 - 80h^{-1} \text{ Mpc}$	45

Table 2. Summary of large-scale cuts used in recent Stage III $3\times 2\text{pt}$ analyses and the corresponding values of ℓ_{min} . The range in ℓ_{min} values in the bottom entries for KiDS and HSC come from converting fixed length scale cutoff R to corresponding angular multipole for different redshift bins.

the galaxy clustering and galaxy-galaxy lensing probes following the harmonic space scale cuts from the DESC SRD (The LSST Dark Energy Science Collaboration 2018). This corresponds to a minimum physical scale cut of $k_{\text{max}} = 0.3h/\text{Mpc}$, limited by the modeling of non-linearities and baryonic effects in the galaxy power spectrum. For cosmic shear, the DESC SRD used $\ell_{\text{max}} = 3000$, which is more aggressive than previous work; we choose to adopt a more conservative cut of $\ell_{\text{max}} = 500$ for our fiducial analysis. Later we explore the impact of extending the LSST analysis to smaller length scales.

3.2 Gravitational Wave Samples

For the GW samples, we include gravitational waves produced by coalescing binary black holes, black hole/neutron star binaries, and binary neutron stars. We expect these events to occur in galaxies, as they are home to the most intense star formation, implying that the distribution of GWs is expected to follow that of the underlying dark matter large-scale structure (Bosi et al. 2023).

We describe each GW sample using three parameters that are determined by the chosen detector setups: the number of GW detections per year, their sky localization precision, and the redshift range of the detected sources. The number of detections n_{GW} determines the shot noise contribution to the clustering power spectrum – the number density of predicted GW events is orders of magnitude lower than that of galaxies in photometric surveys, which leads to a higher contribution from shot noise. The precision with which GW events can be localized on the sky determines the minimum angular scale (maximum ℓ) on which the clustering of GW events can be inferred. Lastly, the redshift range (and precision) determines the cosmological information contained in the GW source clustering. Redshift range overlap between the GW and LSST sources is beneficial, as it potentially strengthens the constraints on galaxy bias for both sets of sources. In addition, for future GW detector networks with high sensitivity, a large fraction of GW events are predicted to be concentrated at higher redshifts – the peak of the forecast GW $n(z)$ distribution is at $z \sim 2$, since this is the redshift at which the star formation rate peaks, and a significant fraction of events occur at even higher redshift.

We define three GW setups of increasing optimism, with different values for the detector network parameters n_{GW} , ℓ_{max} , and z range. The values of these parameters are listed in Table 3, and the corresponding redshift bins are shown in the right panel of Fig. 2.

Setup 1 is the least optimistic, as it assumes a relatively low number density of events, moderate spatial localization (ℓ_{max}) and limited z range. It corresponds roughly to a third generation (3G) GW detector network comprising the Einstein Telescope (ET, Maggiore et al. 2020), Cosmic Explorer (Reitze et al. 2019), and LIGO Voyager (Adhikari et al. 2018). We estimate this network to have localization precision such that $\ell_{\text{max}} = 30$ over the redshift range $0 < z < 0.5$, a median luminosity distance uncertainty of $\sim 13\%$, and 10^4 detections/year. (Hall & Evans 2019; Borhanian & Sathyaprakash 2022).

Setup 3 considers the ideal case in which all events are detected with extremely good localization; it is approximately based on a network composed of three ET-like third generation telescopes. We use a GW detection rate of 10^6 events/year, with a $\sim 5\%$ uncertainty in luminosity distance (Maggiore

et al. 2020). Using values computed in Namikawa et al. (2016), we define Setup 3 to cover the redshift range $0 < z < 3$, with $\ell_{\max} = 90$ over the redshift range $0 < z < 1.3$ and $\ell_{\max} = 57$ for $1 < z < 3$. Setup 2 is a middle scenario between 1 and 3, with 10^5 detections/year, redshift range of $0 < z < 1.3$, and localization allowing for analysis of scales with $\ell < 60$ over this range.

The redshift binning of Setup 1 comprises three bins over the range $0 < z < 0.5$. Setup 2 contains the three Setup 1 bins, as well as an additional nine covering the range $0.4 < z < 1.3$. Setup 3 is composed of the twelve Setup 2 bins and 8 more bins over the range $1 < z < 3$. The right panel of Fig. 2 shows these distributions (the details of how they are constructed are given below). Although the lower assumed uncertainty in luminosity distance in Setup 3 would allow us to use finer redshift binning over the range $1 < z < 3$, testing has shown that in our analysis a greater proportion of cosmological information is contained in the $z \lesssim 1$ range than at higher redshift. Additionally, overlap between the GW and LSST redshift bins improves constraining power, and the LSST redshift distributions reside mostly in the $0 < z < 1.5$ range. A larger number of GW redshift bins also increases computational complexity and decreases the number density of objects in each bin; the three sets of GW $n(z)$ bins we propose represent a happy medium between fine binning of the lower- z range and computational complexity.

To generate the total GW redshift distribution, we assume that the number density of GW sources is proportional to the star formation rate described in Madau & Dickinson (2014). The star formation rate function $R_{\star}(z)$ is used to compute the number of events expected at varying masses and redshifts:

$$R_{\star}(z) = \frac{(1+z)^{2.6}}{1 + \left(\frac{1+z}{3.2}\right)^{6.2}}, \quad \frac{dn}{dz} = A_s R_{\star}(z) \frac{V_c(z)}{1+z}, \quad (11)$$

where V_c is the differential comoving volume and A_s normalizes to the fraction of stellar mass that is converted to GW sources and our chosen number of detections per year. It is relevant to note that the GW formation channel affects the time delay between progenitor star formation and binary coalescence, and therefore the shape of the GW $n(z)$ distribution. Our model assumes this time delay is relatively short (< 1 Gyr), which Fishbach & Kalogera (2021) finds is favored in all formation channels they consider.

Additionally, we assume that in the z ranges of our setups, the detection rate of events is not dependent on redshift. GW events within these ranges have a signal to noise ratio above the detection threshold for all networks considered (Borhanian & Sathyaprakash 2022), therefore we assume a fixed fraction are detectable independent of redshift.

The binning choice of the GW redshift distribution is dependent on the parameters of the chosen detector setup. We

divide the redshift range for a particular setup into n_{bins} subintervals such that each subinterval contains an equal number of GW events drawn from the total $n(z)$ distribution. To transform these true redshift distributions into the observed distributions, we convolve the distribution in each subinterval with a Gaussian of width $\sigma(z)$ determined by the detector's redshift uncertainty as inferred from the above uncertainty in luminosity distance. This generates the set of n_{bins} redshift distributions shown in Fig. 2.

Number density is determined based on the detection rate of the chosen network. We calculate the fraction of total events contained in each z range and divide by the number of bins within that range, giving the fraction of events contained within each individual (equipopulated) bin. Multiplying by the yearly detection rate with ten years of observation and dividing by the observed area (in this case, the full sky) gives us the number density of events per bin. For use with `jax_cosmo`'s differentiable functionality, we convert the binned distributions to small approximations described by smooth functions. The area under the curve of each bin is normalized to unity and then multiplied by the number density scalar.

The fiducial large-scale bias for the GW sources is computed for the median redshift of each bin using this parameterization

$$b_{\text{GW}} = 1.20(1+z)^{0.59}, \quad (12)$$

from Peron et al. (2023), who extract tracer power spectra from mock data-sets of GW events and fit them to a model of the true power spectrum. The result is the above estimated bias. The power spectrum model used in this case neglects third order and scale-dependent contributions, assuming only contributions from the local matter field. The same bias parameterization is assumed in all of our setups. Bias evolution with redshift (as well as time delay between star formation and binary coalescence) depends on the formation channel that leads to GW events, which is currently uncertain – in Section 4.3.2 we test the impact of other choices for the GW bias.

We generate the GW clustering angular power spectrum using the same `jax-cosmo` framework as for LSST. This same software also computes the cross-covariance between the GW $C(\ell)$ arrays and the 3×2 pt probe from LSST.

3.3 Forecasting procedure

We perform a Fisher forecast for the constraining power of the different probes under different setups. The Fisher matrix elements in parameter space are defined by

$$\mathbf{F}_{mn} = \sum_{l_1, l_2} \frac{dC(\ell)_{l_1}}{dp_m} (\mathbf{C}^{-1})_{l_1 l_2} \frac{dC(\ell)_{l_2}}{dp_n}, \quad (13)$$

GW Setup				
Bins	n_{GW} (arcmin $^{-2}$)	ℓ range	z_{peak}	b_{GW}
Setup 1				
1	1.14×10^{-5}	$2 < \ell < 30$	0.27	1.31
2	"	"	0.36	1.44
3	"	"	0.43	1.48
Setup 2				
	n_{GW}	ℓ range	z_{peak}	b_{GW}
1-3	1.14×10^{-4}	$2 < \ell < 60$		
4	1.6×10^{-4}	$2 < \ell < 60$	0.48	1.57
5	"	"	0.59	1.60
6	"	"	0.70	1.64
7	"	"	0.79	1.69
8	"	"	0.86	1.73
9	"	"	0.93	1.77
10	"	"	0.98	1.80
11	"	"	1.04	1.83
12	"	"	1.25	1.94
Setup 3				
	n_{GW}	ℓ range	z_{peak}	b_{GW}
1-3	1.14×10^{-3}	$2 < \ell < 90$		
4-12	1.6×10^{-3}	$2 < \ell < 90$		
13	4.2×10^{-3}	$2 < \ell < 57$	1.43	2.03
14	"	"	1.60	2.11
15	"	"	1.75	2.19
16	"	"	1.91	2.26
17	"	"	2.06	2.33
18	"	"	2.22	2.50
19	"	"	2.40	2.58

Table 3. Binning, GW source number density, ℓ -range, peak redshift, and fiducial GW host bias for the three GW setups. In Setup 3, the ℓ -range for lower- z bins is extended to $2 < \ell < 90$, whereas the higher- z bins only go up to ℓ of 57. Number densities are normalized to ten years spent observing. $n(z)$ distributions are plotted in Fig. 2.

where (\mathbf{C}^{-1}) is the inverse of the covariance matrix, and $dC(\ell)_{l_1}/dp_m$ is the derivative at point l_1 in the $C(\ell)$ data vector (which includes all angular and cross power spectra, including across redshift) with respect to parameter p_m . In the fiducial case, \mathbf{F} has dimension $(n_{\text{cosmo params}} + n_{\text{LSST lens bins}} + n_{\text{GW bins}})^2$, since there is an undetermined galaxy bias parameter for each LSST lens and GW redshift bin, and $n_{\text{cosmo params}} = 5$ (Λ CDM) or 6 (w CDM or f_{NL} extension). We do not consider other nuisance parameters, such as those related to the $n(z)$ distributions or the shear multiplicative bias. Thus, our results assume those systematics are subdominant.

We construct the Fisher matrix from Jacobian and covariance matrices. Since we use the differentiable `jax-cosmo` framework to generate the angular power spectra, it is trivial to perform these derivatives in a stable way. The (l_1, m) th term of the Jacobian matrix is defined as

$$\mathbf{J}_{lm} = \frac{\delta C(\ell)_{l_1}}{\delta p_m}, \quad (14)$$

for the l th value in the $C(\ell)$ array and varied parameter p_m .

We first compute one covariance and one Jacobian matrix containing all LSST Y10 lens, LSST Y10 source, and GW probes, spanning the range $2 < \ell < 3000$ and using an

f_{sky} of 1. We then apply cuts to remove data points/indices corresponding to LSST lens and source bins that do not fall within the actual ℓ cuts given in the tables above. The covariance matrix terms of all LSST-associated data points assume $f_{\text{sky}} = 0.3466$ whereas those of GW-associated data points assume $f_{\text{sky}} = 1$.

We compute the Figure of Merit (FoM) as

$$\text{FoM}_\theta = \frac{1}{\sqrt{\det[(\mathbf{F}^{-1})_\theta]}}, \quad (15)$$

where \mathbf{F}^{-1} is the inverted Fisher matrix of all parameters varied in the analysis (cosmological and galaxy bias), and θ represents the selection of parameters to be considered in the FoM.

4 RESULTS

In this section, we present the main results from this study. Sec. 4.1 discusses Λ CDM and w CDM results for the baseline LSST 3 \times 2pt analysis, for the LSST analysis extended to very large scales, and for the baseline LSST analysis augmented by GW clustering on very large scales. Sec. 4.2 extends the results to PNG and constraints on f_{NL} . In Sec. 4.3, we vary some of our analysis choices to determine the impact of these setup changes and assumptions on our results. These variations include the LSST scale cuts (4.3.1) as well as GW galaxy bias (4.3.2) and GW scale cuts (4.3.3).

4.1 Λ and w CDM

Here we present the results for the Λ CDM and w CDM models. For now, we only consider the most optimistic case for the GW detector network (GW setup 3).

As an example, Figure 4 shows results for 3 different setups in the context of the w CDM model: the baseline LSST Y10 3 \times 2pt analysis (green), the LSST analysis extended to very large scales, $\ell > 2$ (purple), and the LSST baseline combined with GW source clustering in setup 3 (light blue). The relative gains in precision of cosmological constraints for the latter two cases relative to the LSST baseline are given in Table 4 for both Λ CDM and w CDM. For w CDM, the addition of the very large scales ($2 < \ell < 50$) to the baseline LSST Y10 3 \times 2pt analysis leads to a fractional improvement in the parameter constraints of between 2.8 and 6.2%. The Λ CDM results are qualitatively similar. Note that these results assume that residual systematic effects on very large scales ($\ell < 50$) in LSST will be negligible.

By comparison, combining the baseline LSST analysis with GW clustering at large scales improves parameter constraints over the baseline LSST analysis by less than 1%. This difference is not surprising, as even in the optimistic GW setup,

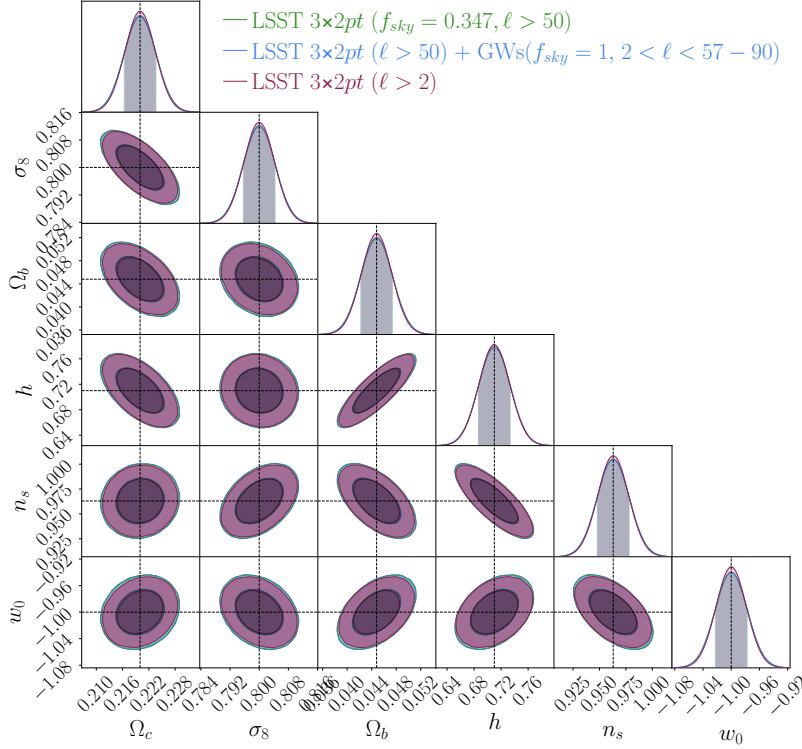


Figure 4. Marginalized 68% and 95% CL w CDM constraints from LSST 3 \times 2pt baseline analysis (green), LSST 3 \times 2pt extended to very large scales (purple), and LSST baseline plus GW auto-correlation on very large scales (light blue). Differences between these are quantified in Table 4.

the shot noise is much larger than for LSST (see Fig. 3). However, the neglect of systematic effects in the very large-scale GW measurements appears to be better justified than for LSST.

Another result of this combined analysis is that in the Λ CDM model we are able to constrain the 19 GW source galaxy bias values to between 2.7% (GW bin 1) and 12% (GW bin 19) precision. This contrasts with a much larger $\sim 218\%$ precision in GW galaxy bias from GW clustering alone, due to the degeneracy between σ_8 and GW host bias. We find similar results for w CDM, with precision between 2.8% (GW bin 1) and 12% (GW bin 19) from LSST + GW and 245% from GW alone. This is particularly interesting as constraining the galaxy bias of GW sources is an active area of study and can help us understand the galaxy populations that host GW events and thus GW formation pathways (Vijaykumar et al. 2023; Mukherjee et al. 2021).

In the last three columns of Table 4, we explore the impact on parameter constraints and on the gain from adding very large scale measurements if we adopt more aggressive small-scale analysis cuts in the context of w CDM. For cosmic shear, $\ell_{\text{max}}^{\text{src}}$ is increased from 500 to 3000, and for clustering and galaxy-shear the maximum wavenumber is increased from 0.3 to $0.6h/\text{Mpc}$. The inclusion of smaller scales increases the constraining power of the baseline LSST Y10 analysis, reduc-

ing the relative improvement from measurements on very large scales: for w CDM, the addition of LSST 3 \times 2pt large scales improves constraints on cosmological parameters by 0.9-2.6% and addition of GWs by 0.04-0.5%. Results for Λ CDM are similar.

4.2 Primordial non-Gaussianity and f_{NL}

Here we present results for the Λ CDM model with primordial non-Gaussianity characterized by f_{NL} . Using the same setup as in Sec. 4.1, we first consider the most optimistic case for the GW detector network (GW setup 3). We then explore in Sec 4.2.2 how changing the setup affects the results.

4.2.1 Large scales and f_{NL}

Fig. 5 shows the constraints on the Λ CDM+ f_{NL} parameters from the baseline LSST Y10 3 \times 2pt alone (green), with the addition of GW clustering on large scales (blue), and with the addition of LSST 3 \times 2pt analysis on large scales (purple). The baseline constraints on the Λ CDM parameters are slightly weaker than those in Table 4 due to the marginalization over f_{NL} . We see that the addition of information from very large scales ($\ell < 50$), either from LSST or GW, dramatically improves the constraint on f_{NL} – from $\sigma(f_{\text{NL}}) = 76.5$

Parameter	Percent Improvement on Parameter Constraints						w CDM: $\ell_{\max}^{\text{src}} = 3000, k_{\max}^{\text{lens}} = 0.6$		
	Λ CDM			w CDM			Λ CDM		
	$\sigma(\text{param})$	+ 3 \times 2pt L.S.	+ GWs	$\sigma(\text{param})$	+ 3 \times 2pt L.S.	+ GWs	$\sigma(\text{param})$	+ 3 \times 2pt L.S.	+ GWs
Ω_c	0.0036	6.1%	0.98%	0.0037	5.1%	0.78%	0.0023	2.2%	0.48%
σ_8	0.0052	3.9%	0.36%	0.0055	3.6%	0.19%	0.0017	2.6%	0.32%
Ω_b	0.0023	2.6%	0.61%	0.0027	4.9%	0.78%	0.0020	2.3%	0.52%
h	0.022	1.1%	0.24%	0.0025	2.8%	0.40%	0.014	0.87%	0.25%
n_s	0.014	1.4%	0.09%	0.018	4.1%	0.30%	0.0057	0.91%	0.04%
w_0	-	-	-	0.023	5.9%	0.40%	0.014	2.3%	0.14%
LSST b_{gal} bin 1	0.0093	3.9%	0.42%	0.010	5.0%	0.60%	0.0043	3.58%	0.41%
LSST b_{gal} bin 10	0.0097	4.8%	0.58%	0.016	7.0%	0.83%	0.0091	3.08%	0.28%

Table 4. Marginalized 68% CL parameter constraints ($\sigma(\text{param})$) from LSST Y10 3 \times 2pt baseline ($\ell > 50$) and percent improvement in constraints on parameters with addition of LSST measurements on large scales ($\ell = 2 - 50$, denoted +3 \times 2pt L.S.) or with addition of GW clustering analysis on large scales ($\ell = 2$ to $57 - 90$ with ℓ_{\max} depending on redshift bin.) for Λ CDM and w CDM. For LSST b_{gal} , we present statistics for redshift bins 1 and 10 to show the range of values produced. For comparison, last three columns show parameter constraints and improvements when the cosmic shear, galaxy-shear, and galaxy clustering measurements are extended to smaller scales in w CDM (see text).

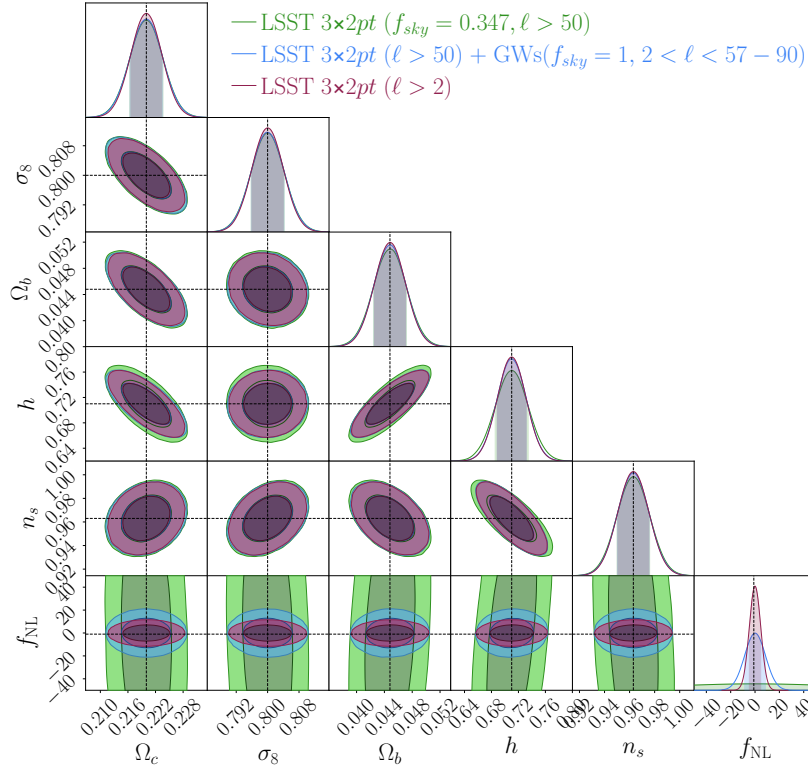


Figure 5. Marginalized 68% and 95% CL constraints on cosmological parameters in Λ CDM including PNG parameterized by f_{NL} . The three analysis setups are identical to those in Fig. 4.

to $\sigma(f_{\text{NL}}) \simeq 8.5$ for GWs and $\sigma(f_{\text{NL}}) \simeq 4.6$ for LSST large scales. This is not surprising, given that the scale-dependent bias in the PNG model grows at large scale. (Some previous works have found LSST galaxy clustering alone to provide tighter constraints on f_{NL} (e.g. Moradinezhad Dizgah & Dvorkin 2018; Green et al. 2023) due to either using a lower ℓ_{\min} or marginalizing over fewer parameters than we do here.) Fig. 5 also shows that the addition of very large scale information noticeably improves the constraints on the Hubble

parameter h ; this is discussed further in Sec. 4.3.1.

Although the extension of the LSST 3 \times 2pt analysis to very large scales yields tighter statistical constraints than the addition of GW clustering, as noted above we expect the latter to be much more robust to systematic errors.

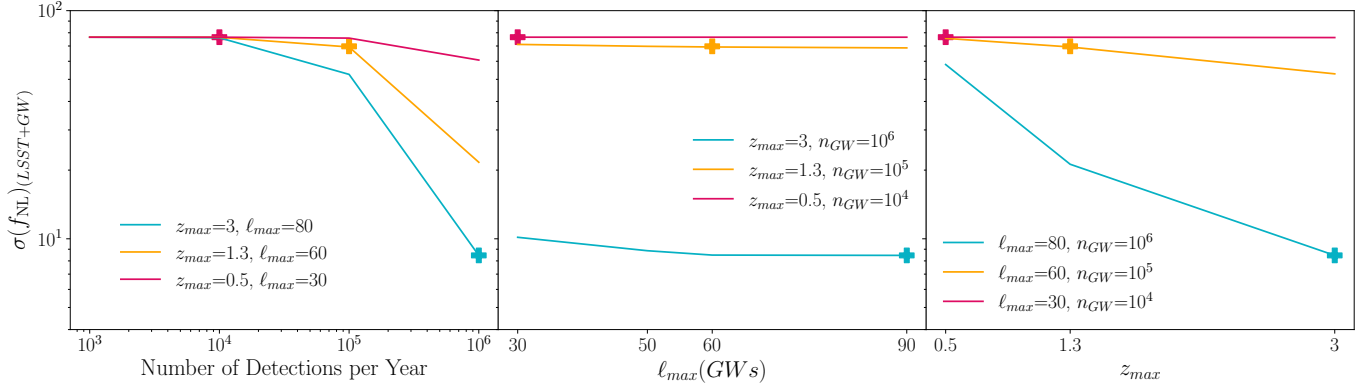


Figure 6. Marginalized 68% CL uncertainty on f_{NL} with LSST baseline plus varying GW setups. Points marked with a \oplus indicate the base parameters of the 3 GW setups (see text).

4.2.2 Dependence on GW detector network parameters

Fig. 6 shows how the uncertainty on f_{NL} depends on GW setup. Of the three GW detector network parameters we vary, the number of detections per year and the redshift range significantly impact the constraining power on f_{NL} , while ℓ_{max} (GWs) is relatively unimportant. Once n_{GW} increases above $\sim 10^5$ detections/year, the drop in shot noise is such that the large-scale GW clustering measurement provides a useful constraint in combination with LSST. Additionally, we find that z_{max} of at least ~ 1.3 is required for GW clustering to add significant constraining power. For reference, the LSST Y10 lenses have z_{max} of ~ 1.4 . This is important for multiple reasons – having more GW redshift bins allows for more cross-bin correlation and therefore tighter constraints, and higher z_{max} also means more overlap with LSST and a larger fraction of total GW events captured. At z_{max} of 1.3, GWs cover nearly the entire LSST lens range and most of the LSST source range. However, increasing z_{max} to 3 allows us to include 8 more redshift bins and many more GW events – the peak of the GW $n(z)$ distribution is around $z = 2$. By contrast, we find that better localization of events and therefore higher ℓ_{max} has minimal effect on constraining power. This is because most information on f_{NL} is found at extremely large scales.

4.3 Sensitivity of results to analysis choices

We now investigate how changes in the LSST large- and small-scale cuts, the assumed galaxy bias of GW sources, and the GW large-scale cut would affect our results.

4.3.1 LSST scale cuts

Since the maximum angular scale reachable by LSST $3 \times 2\text{pt}$ analysis is not entirely certain, we investigate how different values of $\ell_{\text{min}}(\text{LSST})$ would impact our results. We sum-

marize the results in Fig. 7. As expected, raising $\ell_{\text{min}}(\text{LSST})$ reduces the total amount of information gathered, and vice versa. Constraints on f_{NL} already come almost entirely from the GW clustering, so raising $\ell_{\text{min}}(\text{LSST})$ has little impact on the f_{NL} uncertainty after the addition of GWs. As an example, constraints using $\ell_{\text{min}}(\text{LSST}) = 90$ are listed in Table 5. Note that $\ell_{\text{min}}(\text{LSST})$ is determined independently of $\ell_{\text{max}}(\text{GW})$, so changes in the former are not implicitly referring to changes in the latter. Thus, the range of scales for LSST are allowed to overlap that of the GWs.

In Fig. 7 we see different sensitivities of the ΛCDM parameters to the LSST large-scale cut. In particular, as $\ell_{\text{min}}(\text{LSST})$ increases, the addition of GW information has greater relative impact upon the constraints on Ω_c , Ω_b , h , and b_{gal} (i.e., the gap between LSST only and LSST + GW points increases). This greater dependence on large scales is due in part to the relation of $\Omega_m (= \Omega_c + \Omega_b)$ and h to the location of the peak of the 3D power spectrum, k_{peak} . To see this, we note that the value of k_{peak} is close to the comoving value of k_{eq} , the inverse Hubble scale at the time of matter-radiation equality, and k_{eq} is proportional to $(\Omega_m h^2)^{1/2}$. For the fiducial ΛCDM parameters, $k_{\text{peak}} \approx 0.0187 h/\text{Mpc}$, which for the LSST redshift range corresponds to $\sim 20 < \ell < 80$. Further information on Ω_b and Ω_c is also found at higher k , but h is particularly dependent on large scales, which is why we see GWs impact constraints most prominently in the h plot of Fig. 7, and in the h contours of Fig. 5. In contrast, we see that σ_8 and n_s are much less reliant on large scales—removing LSST information on large scales does not cause the addition of GW large-scale information to become more impactful.

We also test the impact of more aggressive small-scale cuts for the LSST sources and lenses. Results for $k_{\text{max}}^{\text{lens}} = 0.6 h/\text{Mpc}$, $\ell_{\text{max}}^{\text{src}} = 3000$ are listed in Table 5 (column 4), and results for a range of $(k_{\text{max}}^{\text{lens}}, \ell_{\text{max}}^{\text{src}})$ values are shown in Fig. 8. Little information on f_{NL} is found at small scales, so while a more

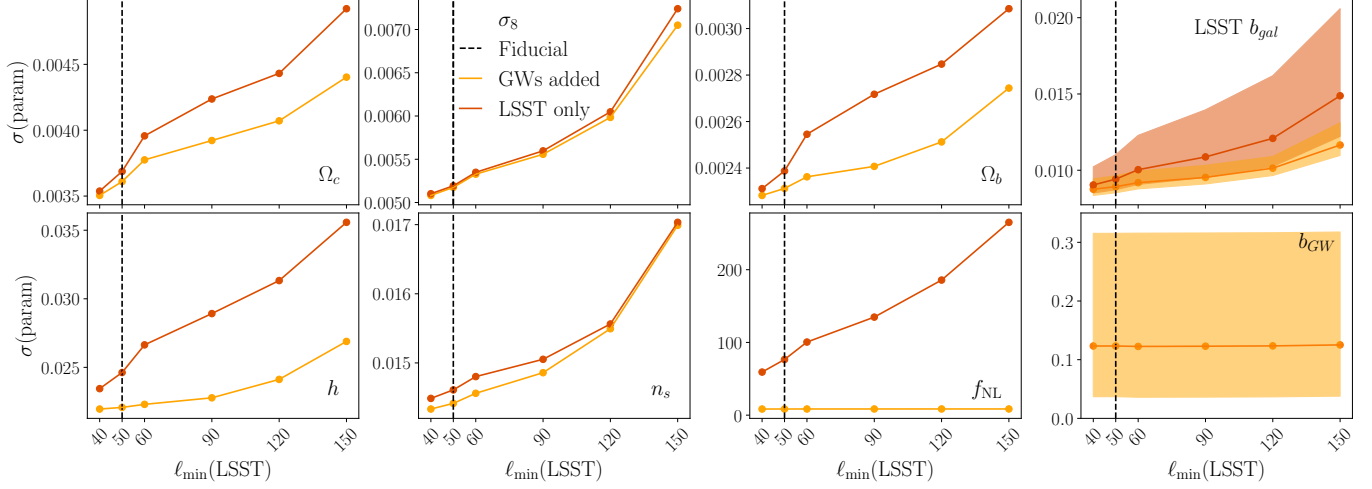


Figure 7. Effect of varying $\ell_{\min}(\text{LSST})$ on constraining power from LSST 3 \times 2 pt with (yellow) and without (red) GW, for cosmological parameters in $\Lambda\text{CDM}+f_{\text{NL}}$. For the LSST and GW bias plots, solid lines show the average value and shaded areas show the range of values across redshift bins. The fiducial setup throughout the paper is $\ell_{\min}(\text{LSST}) = 50$, indicated by the vertical dashed line in each column. All analyses use GW Setup 3 ($0 < z < 3$, $2 < \ell < 57 - 90$ with ℓ_{\max} depending on redshift bin.).

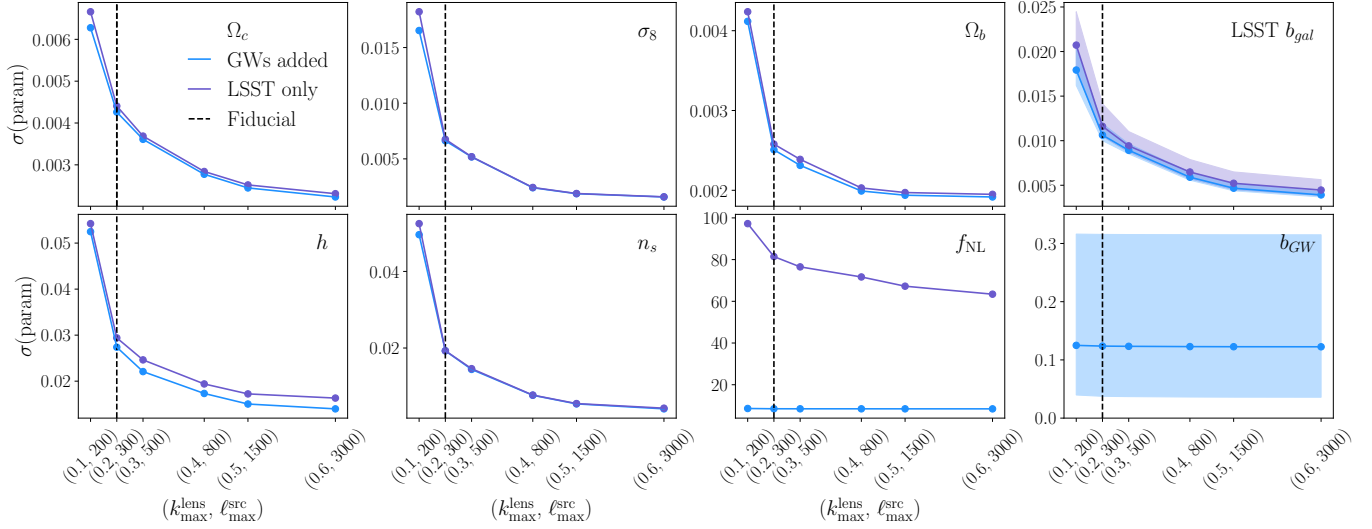


Figure 8. Effect of varying k_{\max}^{lens} and ℓ_{\max}^{src} on constraining power for cosmological parameters in $\Lambda\text{CDM}+f_{\text{NL}}$ for LSST 3 \times 2 pt with (blue) and without (purple) GW. For the LSST and GW bias plots, solid lines show the average value and shaded areas show the range of values across bins. The fiducial values throughout the paper are $k_{\max}^{\text{lens}} = 0.3h/\text{Mpc}$ and $\ell_{\max}^{\text{src}} = 500$. All analyses use GW Setup 3 ($0 < z < 3$, $2 < \ell < 57 - 90$ with ℓ_{\max} depending on redshift bin.).

aggressive small-scale cut strengthens the constraints on the other ΛCDM parameters, the impact on f_{NL} from adding GWs is insensitive to this change.

4.3.2 Bias of GW-source host galaxies

Given the relatively small number of GW events to date, the bias for the host galaxies of GW sources is not yet well

understood. While the parameterization for b_{GW} adopted in our analysis above is reasonable, it is important to test the impact on our results of a change in the galaxy bias values for the GW sources. We consider two alternative GW galaxy bias models to the fiducial model of Eqn. 12:

$$\begin{aligned} b_{\text{GW}1} &= 1.20(1+z)^{0.59} + 3, \\ b_{\text{GW}2} &= 2.0. \end{aligned} \quad (16)$$

Impact of Varying Analysis Choices						
	Fiducial	$\ell_{\min}^{\text{LSST}}=90$	$k_{\max}^{\text{src}}=0.6, \ell_{\max}^{\text{lens}}=3000$	GW bias = b_{GW1}	GW bias = b_{GW2}	$\ell_{\min}^{\text{GWs}}=5$
Relative constraining power: FoM(+GWs)/FoM(LSST)						
$\Omega_c, \sigma_8, \Omega_b, h, n_s$	1.09	1.16	1.07	1.38	1.09	1.08
$\Omega_c, \sigma_8, \Omega_b, h, n_s, f_{\text{NL}}$	6.95	9.13	4.70	45.3	6.33	4.72
LSST b_{gal}	1.01	1.01	1.01	1.06	1.01	1.01
Uncertainty on single parameters using LSST+GW						
$\sigma(f_{\text{NL}})$	8.46	8.49	8.43	1.56	9.31	14.2
$\sigma(b_{\text{GW}})$, bin 1	0.037	0.038	0.036	0.061	0.041	0.037
$\sigma(b_{\text{GW}})$, bin 10	0.091	0.092	0.91	0.090	0.090	0.092
$\sigma(b_{\text{GW}})$, bin 19	0.32	0.32	0.31	0.22	0.37	0.32

Table 5. Statistics describing the effect on our results of varying analysis choices. Upper 3 rows: ratio of figure of merit values, $\text{FoM}(params)_{\text{LSST+GW}}/\text{FoM}(params)_{\text{LSSTonly}}$, for $params = [\Omega_c, \sigma_8, \Omega_b, h, n_s]$ (Λ CDM), $params = [\Omega_c, \sigma_8, \Omega_b, h, n_s, f_{\text{NL}}]$ (Λ CDM + f_{NL}), and $params = [\text{LSST lens galaxy bias values}]$. Lower 2 rows: $\sigma_{\text{LSST+GW}}(param)$ values for f_{NL} and for a range of GW galaxy biases, for Λ CDM + f_{NL} . All statistics use a GW setup with the redshift and ℓ range of Setup 3 ($0 < z < 3, 2 < \ell < 57 - 90$ with ℓ_{\max} depending on redshift bin.).

These alternatives represent 1) a bias model with the same shape as the fiducial bias model but shifted to a higher value as a conservative upper limit, and 2) a model with a constant (redshift-independent) bias approximately equal to the average of the fiducial values. For model b_{GW1} , the bias of GW sources is very large, leading to a higher clustering amplitude and tighter constraints on Λ CDM parameters from the combination of LSST and GW compared to the fiducial case. Moreover, in this case, the amplitude of the scale-dependent bias due to f_{NL} is larger (see Eqn. 8), leading to significantly stronger constraints on f_{NL} than for the fiducial case—for example, in going from the fiducial b_{GW} to b_{GW1} , $\sigma(f_{\text{NL}})$ improves from 8.46 to 1.56. These results are shown in Table 5, columns 5 and 6.

4.3.3 GW scale cuts

While an $\ell_{\min}(\text{GWs})$ value of 2 is reasonable given GW detectors survey the full sky, we investigate whether the clustering of GW sources would still provide improvement to constraints from LSST 3 \times 2pt if the analysis could not be performed on the largest scales. As expected, the loss of the largest scales decreases constraining power on f_{NL} , but we find that even with $\ell_{\min}(\text{GWs}) = 5$, GWs still provide a significant improvement (Table 5, column 7).

5 CONCLUSIONS

In this work, we have studied the cosmological information that can be extracted from two-point correlation measurements on very large scales, focusing on the clustering of gravitational wave (GW) sources and its combination with two-point measurements from optical galaxy surveys on intermediate to large scales. The advantages of using GW detectors at the largest scales is that their angular selection function is well understood, they are sensitive to events over the full sky, they can extend to high redshifts, and the distance error per event is

relatively small; moreover, they are not subject to the kinds of spatially varying observational and astrophysical systematics that afflict optical surveys on large angular scales. The disadvantages of using GW sources are the relatively low number density of sources (and therefore high shot noise) and poor sky localization (and therefore lack of small-scale information) compared to optical surveys. Given these relative advantages and disadvantages, we have explored the potential benefits to combining GW and optical survey measurements in a complementary way. We investigated the problem in the context of Λ CDM, w CDM, and Λ CDM + f_{NL} and considered the combination of several future GW detector setups with projected LSST Y10 \times 2pt measurements, varying a number of assumptions about the analysis.

Our main findings are the following:

- In Λ CDM and w CDM, there is no significant information gain (improvement in cosmological parameter constraints) from clustering on very large scales ($\ell < 50$). However, the LSST+GW combination does enable us to constrain the redshift-dependent bias of the host galaxies of GW sources to an average $\sim 6\%$ precision, which is a currently largely unknown quantity.
- For Λ CDM + f_{NL} , the addition of very large-scale information, either from LSST 3 \times 2pt or the clustering of GW sources, results in a roughly order of magnitude improvement in the constraint on f_{NL} , with $\sigma(f_{\text{NL}}) = 8.8$. For GW to be competitive, the network of detectors must have sensitivity to detect more than 10^5 events per year out to redshifts up to $z \sim 3$. We also find that including GW analysis of the range $30 < \ell < 90$ is relatively unimportant, as information on f_{NL} is found at even larger scales, and LSST already provides sufficient information on the $50 < \ell < 90$ range in the baseline analysis.
- Changes to the scale cuts in the LSST 3 \times 2pt analysis, to

parameterization of the GW bias, and to the scale cuts on the GW analysis do not significantly affect the forecast constraints on the Λ CDM parameters. However, we find that a change in the GW bias parameterization can change the projected constraints on f_{NL} significantly, due to the relationship between f_{NL} and galaxy bias.

With the upcoming wealth of data expected from a number of optical/NIR galaxy surveys (LSST, Euclid, Roman) and GW experiments (Einstein Telescope, Cosmic Explorer and LIGO Voyager), we will soon enter a regime where cleverly combining different datasets could allow us to tackle some of the systematic effects that are challenging to address in a single survey. Here we have investigated how using GW sources as LSS tracers can evade the large-scale systematic effects in optical galaxy surveys, but it is likely that these combinations would have other benefits worth studying, just as there have been many applications of combining galaxy and CMB datasets in the past 10 years (Schaan et al. 2017; Abbott et al. 2023). The combination of galaxy surveys and GW experiments could have a similar potential, opening up a new area of multi-probe cosmology.

ACKNOWLEDGEMENTS

We would like to especially thank Aditya Vijaykumar for many useful discussions and help with the gravitational waves observations setup. We also thank Daniel Holz, Jose Maria Ezquiaga Bravo, and Hayden Lee for helpful discussions. We thank François Lanusse for help on `jax-cosmo`.

ELG is supported by DOE grant DE-AC02-07CH11359. DA is supported by NSF grant No. 2108168. JP is supported by the Eric and Wendy Schmidt AI in Science Postdoctoral Fellowship, a Schmidt Futures program. CC is supported by the Henry Luce Foundation and DOE grant DE-SC0021949. JF is supported in part by the DOE at Fermilab and in part by the Schmidt Futures program.

REFERENCES

- Abbott T. M. C., et al. 2018, *Phys. Rev. D*, **98**, 043526
- Abbott T. M. C., et al. 2022, *Phys. Rev. D*, **105**, 023520
- Abbott T. M. C., et al. 2023, *Phys. Rev. D*, **107**, 023531
- Achúcarro A., et al. 2022, *arXiv e-prints*, p. [arXiv:2203.08128](https://arxiv.org/abs/2203.08128)
- Adhikari R. X., et al. 2018
- Adhikari S., et al. 2020, *ApJ*, **905**, 21
- Albrecht A., et al. 2006, *arXiv e-prints*, pp astro-ph/0609591
- Anbajagane D., et al. 2023, *arXiv e-prints*, p. [arXiv:2310.02349](https://arxiv.org/abs/2310.02349)
- Aricò G., et al. 2023, *A&A*, **678**, A109
- Balardo A., et al. 2023, *J. Cosmology Astropart. Phys.*, **2023**, 050
- Barreira A., 2020, *J. Cosmology Astropart. Phys.*, **2020**, 031
- Barreira A., 2022, *Journal of Cosmology and Astroparticle Physics*, **2022**, 013
- Bera S., et al. 2020, *The Astrophysical Journal*, **902**, 79
- Borhanian S., Sathyaprakash B. S., 2022, Listening to the Universe with Next Generation Ground-Based Gravitational-Wave Detectors ([arXiv:2202.11048](https://arxiv.org/abs/2202.11048))
- Bosi M., Bellomo N., Raccanelli A., 2023, *arXiv e-prints*, p. [arXiv:2306.03031](https://arxiv.org/abs/2306.03031)
- Byrnes C. T., Choi K.-Y., 2010, *Advances in Astronomy*, **2010**, 724525
- Calore F., et al. 2020, *Physical Review Research*, **2**, 023314
- Campagne J.-E., et al. 2023, *The Open Journal of Astrophysics*, **6**
- Chen H.-Y., et al. 2017, Observational Selection Effects with Ground-based Gravitational Wave Detectors ([arXiv:1608.00164](https://arxiv.org/abs/1608.00164)), [doi:10.3847/1538-4357/835/1/31](https://doi.org/10.3847/1538-4357/835/1/31)
- Chen A., et al. 2023, *MNRAS*, **518**, 5340
- Coulton W. R., et al. 2023, *ApJ*, **943**, 64
- Dalal N., et al. 2008, *Phys. Rev. D*, **77**, 123514
- Dvornik A., et al. 2023, *A&A*, **675**, A189
- Finn L. S., Chernoff D. F., 1993, *Phys. Rev. D*, **47**, 2198
- Fishbach M., Kalogera V., 2021, *The Astrophysical Journal Letters*, **914**, L30
- Green D., et al. 2023, *arXiv e-prints*, p. [arXiv:2311.04882](https://arxiv.org/abs/2311.04882)
- Hall E. D., Evans M., 2019, *Classical and Quantum Gravity*, **36**, 225002
- Heymans C., et al. 2021, *A&A*, **646**, A140
- Ivezić Ž., et al. 2019, *ApJ*, **873**, 111
- Kilbinger M., et al. 2017, *Monthly Notices of the Royal Astronomical Society*, **472**, 2126–2141
- Kobayashi Y., et al. 2022, *Phys. Rev. D*, **105**, 083517
- Lange J. U., et al. 2023, *MNRAS*, **520**, 5373
- Libanore S., et al. 2022, *J. Cosmology Astropart. Phys.*, **2022**, 003
- LoVerde M., Afshordi N., 2008, *Physical Review D*, **78**
- Madau P., Dickinson M., 2014, *ARA&A*, **52**, 415
- Maggiore M., et al. 2020, *J. Cosmology Astropart. Phys.*, **2020**, 050
- Martinelli M., et al. 2021, *A&A*, **649**, A100
- Miyatake H., et al. 2022, *Phys. Rev. D*, **106**, 083520
- Miyatake H., et al. 2023, *arXiv e-prints*, p. [arXiv:2304.00704](https://arxiv.org/abs/2304.00704)
- Moradinezhad Dizgah A., Dvorkin C., 2018, *J. Cosmology Astropart. Phys.*, **2018**, 010
- Mpetha C. T., Congedo G., Taylor A., 2023, *Phys. Rev. D*, **107**, 103518
- Mukherjee S., et al. 2021, *Physical Review D*, **103**
- Namikawa T., Nishizawa A., Taruya A., 2016, *Phys. Rev. Lett.*, **116**, 121302
- Peron M., et al. 2023, Clustering of binary black hole mergers: a detailed analysis of the EAGLE+MOBSE simulation ([arXiv:2305.18003](https://arxiv.org/abs/2305.18003))
- Planck Collaboration 2020, *A&A*, **641**, A9
- Reitze D., et al. 2019, Cosmic Explorer: The U.S. Contribution to Gravitational-Wave Astronomy beyond LIGO ([arXiv:1907.04833](https://arxiv.org/abs/1907.04833))
- Rodríguez-Monroy M., et al. 2022, *MNRAS*, **511**, 2665
- Scelfo G., et al. 2018, *J. Cosmology Astropart. Phys.*, **2018**, 039
- Scelfo G., et al. 2020, *J. Cosmology Astropart. Phys.*, **2020**, 045
- Scelfo G., et al. 2022, *J. Cosmology Astropart. Phys.*, **2022**, 004
- Scelfo G., et al. 2023, *J. Cosmology Astropart. Phys.*, **2023**, 010
- Schaan E., et al. 2017, *Phys. Rev. D*, **95**, 123512
- Schutz B. F., 2011, *Classical and Quantum Gravity*, **28**, 125023
- Shao X., et al. 2022, *Research in Astronomy and Astrophysics*, **22**, 015006
- Sugiyama S., et al. 2023, *arXiv e-prints*, p. [arXiv:2304.00705](https://arxiv.org/abs/2304.00705)
- Takahashi R., et al. 2012, *ApJ*, **761**, 152
- The LSST Dark Energy Science Collaboration 2018, *arXiv e-prints*, p. [arXiv:1809.01669](https://arxiv.org/abs/1809.01669)
- Vijaykumar A., et al. 2023, *Physical Review D*, **108**
- Wechsler R. H., Tinker J. L., 2018, *ARA&A*, **56**, 435
- Yang Q., Hu B., 2023, *Physics of the Dark Universe*, **40**, 101206
- Yuan S., et al. 2022, *MNRAS*, **515**, 871

Zhang Z. J., et al. 2022, *Monthly Notices of the Royal Astronomical Society*, 514, 2181–2197
Zheng Y., et al. 2023, *Phys. Rev. Lett.*, 131, 171403

This paper was built using the Open Journal of Astrophysics L^AT_EX template. The OJA is a journal which provides fast and easy peer review for new papers in the astro-ph section of the arXiv, making the reviewing process simpler for authors and referees alike. Learn more at <http://astro.theoj.org>.